Journal of Colloid and Interface Science 701 (2026) 138682

Contents lists available at ScienceDirect

Journal of Colloid And Interface Science

journal homepage: www.elsevier.com/locate/jcis

Modulating the electronic state of Ni active sites in medium-entropy borides for enhanced water oxidation performance

Yafeng Li [a,1], Lin Wu [a,1], Shuai Chen [a], Meijia Liu [a], Yuhang Lei [a], Shuxin Li [a], Lin Tao [a], Lixiang Li [a], Chengguo Sun [a,b], Han Zhang [a,*], Baigang An [a,*]

[a] Key Laboratory of Energy Materials and Electrochemistry Research Liaoning Province, School of Chemical Engineering, University of Science and Technology Liaoning, Anshan 114051, China
[b] School of Chemical Engineering, Nanjing University of Science and Technology, Nanjing 210094, China

HIGHLIGHTS

- Magnetic-assisted co-assembly synthesizes CoFeNiMnB, overcoming metal immiscibility.
- Delivers ultra-low OER overpotential, low Tafel slope and long-term AEMWE stability.
- Mn modulates Ni sites and entropy, optimizing adsorption and boosting reconstruction.

GRAPHICAL ABSTRACT

ARTICLE INFO

Keywords:
Phase segregation
Electronic state
Medium-entropy boride
Oxygen evolution reaction

ABSTRACT

Medium-entropy materials (MEMs) have attracted significant attention for electrocatalytic water oxidation due to their exceptional physicochemical properties. However, limited efforts have been made to elucidate the origins of their extraordinary activity and the intricacies of their atomic arrangements. Herein, we present a novel magnetic field-assisted interface co-assembly approach for synthesizing CoFeNiMnB nanochains (Mn-MEB), effectively overcoming the immiscibility challenges associated with combining multiple metal elements. The resulting Mn-MEB catalyst exhibits remarkably enhanced oxygen evolution reaction (OER) activity, achieving a low overpotential (η_{10} = 280 mV), a small Tafel slope (76.7 mV dec^{-1}), and excellent stability, thereby outperforming conventional catalysts. Structural characterization and theoretical calculations reveal that synergistic electronic coupling modulates the active Ni centers, optimizing intermediate adsorption energies. Meanwhile, in-situ impedance spectroscopy and potentiodynamic polarization curves revealed that the increase in configurational entropy accelerated surface reconstruction and mitigated phase segregation and transformation, thereby enhancing structural stability. When employed as the anode in an alkaline exchange membrane water electrolyzer, the Mn-MEB catalyst achieves a low cell voltage of 1.58 V at 10 mA cm^{-2} and exhibits exceptional stability, sustaining operation for over 130 h. The insights gained into the interplay among composition, activity, and

* Corresponding authors.
E-mail addresses: hzhang0807@163.com (H. Zhang), bgan@ustl.edu.cn (B. An).
[1] These authors contributed equally to this work.

https://doi.org/10.1016/j.jcis.2025.138682
Received 21 June 2025; Received in revised form 8 August 2025; Accepted 9 August 2025
Available online 12 August 2025

stability in medium-entropy coordination systems provide valuable guidance for the strategic design of catalysts tailored to diverse electrochemical processes.

1. Introduction

Advancing clean and renewable energy technologies is essential for reducing reliance on fossil fuels [1]. In this regard, the OER is a key process underpinning sustainable hydrogen generation and the operation of renewable energy conversion and storage devices, such as water electrolyzers and rechargeable metal-air batteries. Nevertheless, the inherently sluggish kinetics associated with the multi-electron transfer steps in the OER pose significant challenges, restricting catalytic efficiency and the overall energy conversion performance [2]. A key challenge in developing efficient and durable catalysts is their ability to lower energy barriers, accelerate reaction kinetics, and ultimately enhance energy conversion efficiency. Currently, state-of-the-art OER electrocatalysts depend on costly noble metals and exhibit limited stability, restricting the widespread application of OER-based technologies [3]. Therefore, developing cost-effective, high-performance OER electrocatalysts is a crucial and worthwhile endeavor [4]. In response, researchers have explored alternative strategies focused on non-noble metal compounds, such as phosphides [5], sulfides [6,7], nitrides [8,9], carbides [10,11], and borides [12,13], as promising candidates for efficient water-splitting electrocatalysis. Transition metal borides (TMBs) have recently attracted significant attention as promising alternatives to precious metals owing to their high electrical conductivity and robust catalytic activity [14,15]. However, under high oxidation conditions and strong alkaline, TMBs electrocatalysts experience leaching of the metal species from the surface, which induces structural collapse and leads to poor stability [16]. Moreover, the catalytic efficiency of TMBs is primarily governed by how reaction intermediates interact with surface active sites, a process influenced by the electronic configuration and charge distribution at these sites [17,18]. Therefore, controlling charge redistribution at catalytic sites and inhibiting phase separation are effective strategies to tailor the interaction between oxygenated intermediates and the catalyst surface, ultimately enhancing both the activity and durability of the OER process.

Driven by the goal of activating electronic states at catalytic sites, a novel strategy involves constructing complex coordination frameworks by incorporating multiple atomic species into TMBs to enhance their electrocatalytic performance. While previous studies have explored binary and ternary borides, their limited compositional diversity has constrained the comprehensive investigation of catalytic potential [19,20]. Medium-entropy materials (MEMs) leverage their compositionally tunable nature to optimize intermediate binding energies, modulate electronic structures, and introduce lattice distortions, thereby enhancing catalytic performance [1,21]. However, their practical application is hindered by significant challenges, including element segregation, particle coarsening, immiscibility and the high energy of synthesis [22]. Recently, advanced strategies such as magnetic field-assisted wet chemical reduction [23–25] and laser-based synthesis techniques [26] have emerged as promising alternatives. These approaches not only overcome immiscibility challenges but also offer scalable, energy-efficient fabrication pathways while mitigating drawbacks like harsh processing conditions and excessive lattice distortion. Therefore, the development of robust synthesis protocols capable of incorporating a broader range of immiscible elements and revealing their synergistic roles in catalysis is crucial for improving the intrinsic activity of MEM-based catalysts.

Herein, we report a magnetic field-assisted interface co-assembly approach for synthesizing 1D magnetic medium-entropy boride (Mn-MEB) nanochains with uniform diameters, and controllable chain lengths. The Mn-MEB structure, characterized by increased configurational entropy and surface reconstruction, effectively stabilizes the crystal structure and enhances corrosion resistance. Additionally, entropy-driven electronic synergy enhances spin polarization at Ni active sites and raises the Fermi level, collectively fine-tuning the adsorption energies of reaction intermediates and accelerating OER kinetics (Fig. 1a). When used as the anode in AEMWE device, the Mn-MEB catalyst achieves a low cell voltage of 1.58 V at 10 mA cm^{-2} and exhibits remarkable stability, operating continuously for over 130 h. This design strategy not only highlights the potential of medium-entropy borides with tailored morphology but also offers new insights into the development of high-performance OER catalysts.

2. Results and discussion

2.1. Synthesis and characterizations of catalysts

Mn-MEB was synthesized through a magnetic field-assisted interface co-assembly approach to create magnetic medium-entropy boride nanochains in an ice-water bath using sodium borohydride as a boronization agent (**Fig. S1**). The morphology of the as-synthesized samples was examined by scanning electron microscopy (SEM). Fig. 1b-c show numerous nanometer-sized spheroidal structures that are uniformly, arranged in a directional manner. The nanochains have uniform diameters (300 nm) and chain lengths (10 μm). The FE-SEM image of Mn-MEB further reveals that the nanochains possess a tightly knit structure. The Mn-MEB architecture was further analyzed by transmission electron microscopy (TEM). The magnified image (Fig. 1d) shows that each nanosphere is approximately 300 nm, consistent with the SEM images. The inset in Fig. 1e presents the selected area electron diffraction (SAED) pattern, which lacks distinct rings or spots, indicating the amorphous nature of Mn-MEB. This conclusion is further supported by high-resolution transmission electron microscopy (HR-TEM) images in Fig. 1e, which show an absence of lattice fringes. Energy-dispersive X-ray spectroscopy (EDS) elemental mapping in Fig. 1f demonstrates a uniform distribution of Fe, Co, Ni, Mn, and B throughout the grains, with no evidence of elemental segregation (**Table S1**). The presence of boron and the four metals in similar ratios was demonstrated. Additionally, the elements in Mn-MEB were monitored by analyzing the electrolyte composition using inductively coupled plasma mass spectrometry (ICP-MS) (**Table S2**). The findings suggest that the synthesized material is a medium-entropy boride, with no single element being dominant. Furthermore, the MEB, CoFeB, CoNiB and CoB samples, which were synthesized using the same magnetic field-assisted method, exhibit a directional array of nanobead morphology (**Fig. S2–3**). This approach effectively overcomes the challenges associated with immiscible elemental systems, enabling the stable incorporation of multiple metal components into the MEB framework.

X-ray diffraction patterns (XRD) analysis was carried out to examine the structural characteristics of CoFeB, MEB, and Mn-MEB. As shown in Fig. 2a, the broad diffraction peaks between 40° and 50° (2θ) correspond to metal boride phases, indicating the amorphous nature of the synthesized borides-consistent with previous reports [27]. Additionally, X-ray photoelectron spectroscopy (XPS) was utilized to investigate the surface chemical composition and electronic states of the as-synthesized Mn-MEB and MEB samples (Fig. 2b-f). In the comprehensive XPS analysis, the diffraction peaks of the main sample closely aligned with those of the comparison sample. The peaks at approximately 660–635 eV were assigned to Mn 2p, suggesting the successful introduction of Mn in Mn-MEB (Fig. 2b). Fig. 3c illustrates the Mn 2p spectrum of Mn-MEB, featuring two main peaks at 642.3 and 652.4 eV, assigned to Mn $2p_{3/2}$ and Mn $2p_{1/2}$, respectively [28]. Further analysis of the Mn $2p_{3/2}$ peak reveals it can be deconvoluted into components at 641.2 and 645.8 eV,

corresponding to Mn^{3+} and Mn^{4+} oxidation states. In the high-resolution Co 2p spectrum shown in Fig. 2d, a distinct peak appears at 778.2 eV, which aligns closely with the characteristic signature of metallic cobalt (Co—B) commonly found in cobalt boride materials [29]. Additionally, a spin-orbit doublet appearing at 781.4 and 797.1 eV is attributed to oxidized cobalt species, likely arising from surface oxidation of the Mn-MEB material [30]. After peak deconvolution of the Fe 2p region, the spectrum exhibits two spin-orbit doublets: one at 711.8 and 725.5 eV, assigned to Fe^{2+}, and another at 706.8 and 720.2 eV, derived from Fe—B [31]. Furthermore, in the high-resolution Ni 2p spectrum, the primary Ni $2p_{3/2}$ and Ni $2p_{1/2}$ peaks appear at 852.4 and 869.5 eV, respectively, corresponding to metallic nickel within the nickel boride phase. Additional peaks at 856.1 and 873.9 eV are attributed to Ni^{2+} species, indicating the formation of nickel oxide or hydroxide due to surface oxidation upon air exposure (Fig. 2f) [32]. The Ni $2p_{3/2}$ peak for Ni^{2+} in Mn-doped MEB shows a negative shift compared to MEB. Similarly, negative shifts are observed in the Co $2p_{3/2}$ and Fe $2p_{3/2}$ peaks. This observed shift is attributed to the fact that, following Mn incorporation, the Co, Fe, and Ni atoms in Mn-MEB exhibit a more electron-rich environment compared to those in MEB. This suggests that Mn doping effectively tunes the electronic structure of MEB, thereby enhancing the intrinsic electrocatalytic activity by optimizing the adsorption and desorption energies of reaction intermediates at the active sites during the OER [33]. The B 1 s XPS spectrum displays two distinct peaks centered at 187.9 and 192.0 eV, respectively (**Fig. S4**) [34]. The signal observed at 187.9 eV is assigned to boron atoms bonded with metals including Ni, Co, Fe, and Mn. In contrast, the peak appearing at 192.0 eV is associated with boron-oxo species, which result from surface oxidation of metal borides of $NaBH_4$ during the synthesis process [35]. Raman spectroscopy further reveals the bonding states of Mn-MEB and MEB. Both samples exhibit complex stretching vibrations between 502 and 688 cm^{-1}, corresponding to E_g bending and A_{1g} stretching modes of Co—O bonds [36,37]. Notably, a distinct peak emerges at 598 cm^{-1} in Mn-MEB (**Fig. S5**), indicative of new bond formation. Electron

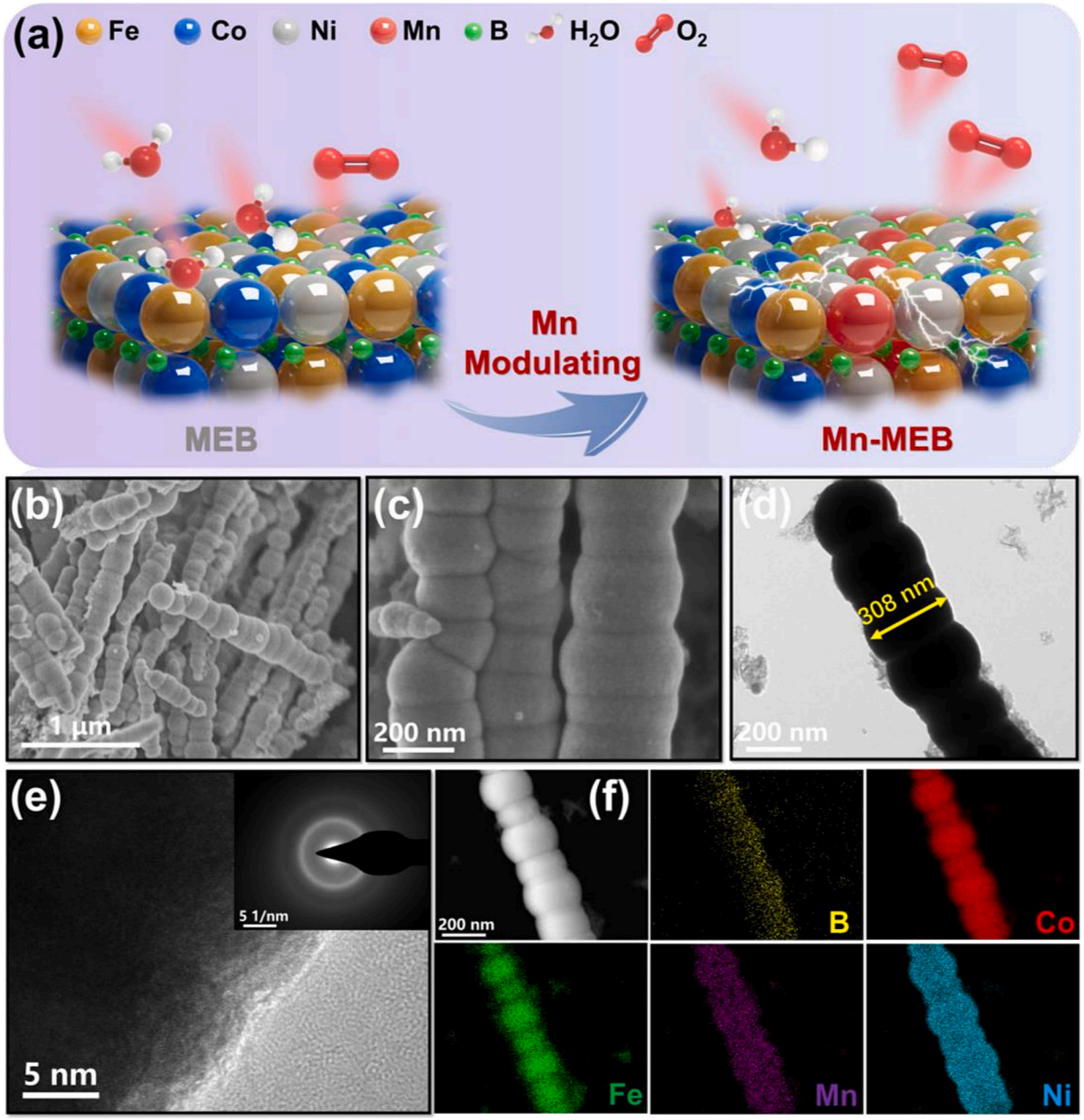

Fig. 1. (a) Schematic illustration of the OER mechanism of Mn modulating MEB. (b-c) SEM images and (d) TEM image of Mn-MEB. (e) HR-TEM image and SAED pattern (inset) of Mn-MEB, (f) HAADF image and elemental mapping results of B, Co, Fe, Mn and Ni.

paramagnetic resonance (EPR) spectroscopy was employed to evaluate the presence of unpaired electrons linked to metal atoms in MEBs after Mn doping. As shown in Fig. 2f, the EPR peak intensity of Mn-MEB is higher than that of the MEB, indicating an increased number of unpaired electrons in Mn-MEB. This enhancement is attributed to the spin state transformation of certain metal atoms induced by Mn incorporation.

2.2. Electrochemical characterization

The OER electrocatalytic performance of samples was assessed in 1 M KOH using a standard three-electrode system. Before conducting linear sweep voltammetry (LSV), the catalyst surfaces were stabilized through 10 cycles of cyclic voltammetry (CV) activation at a scan rate of 10 mV s^{-1} over a potential range of 1.024 to 1.824 V versus RHE (**Fig. S6**). Fig. 3a presents the LSV profiles for Mn-MEB, MEB, CoFeB, and CoNiB electrodes. Among these, Mn-MEB exhibited the best OER activity, requiring an overpotential as low as 280 mV to reach a current density of 10 mA cm^{-2}, outperforming MEB and CoFeB (both at 300 mV) as well as CoNiB (400 mV). This clearly demonstrates that Mn incorporation significantly improves the catalytic efficiency of the novel medium-entropy boride material. Fig. 3b-c **and S7** present Tafel slopes derived from LSV measurements, showing that Mn-MEB exhibits the fastest OER kinetics with the smallest slope of 76.7 mV dec^{-1}, outperforming MEB (97 mV dec^{-1}), CoFeB (102 mV dec^{-1}), and CoNiB (116 mV dec^{-1}). Meanwhile, the influence of Mn-MEB size on the OER catalytic performance was investigated. It was found that the catalytic performance improved with increasing nanobead size (**Fig. S8–10**). Furthermore, Mn-MEB's excellent OER catalytic behavior surpasses that of most recently reported non-precious metal electrocatalysts (**Table S5**). Electrochemical impedance spectroscopy (EIS) was employed to assess the charge transfer properties of the catalysts. As illustrated in Fig. 3d **and S11**, Mn-MEB exhibited the lowest phase angle and charge transfer resistance (R_{ct}) of 8.7 Ω (**Table S4**), indicated by the smallest semicircle on the Nyquist plot, which correlates well with its superior Tafel slope [38,39]. To evaluate the influence of the electrochemically active surface area (ECSA) on electrode performance, the current density was normalized to the ECSA values. According to Fig. 3e and **Fig. S12**, the measured C_{dl} values of Mn-MEB (31.4 mF cm^{-2}) are higher than those of MEB (15.0 mF cm^{-2}). Mn-MEB depicted a relatively high electrocatalytic active area, indicating enhanced remodeling capability and faster catalytic reaction kinetics (**Fig. S13**). A higher turnover frequency (TOF) indicates a more efficient catalyst, capable of producing more oxygen molecules with fewer active sites (**Fig. S14**). The TOF of Mn-MEB reaches 0.49 s^{-1} at an overpotential of 300 mV, significantly exceeding that of undoped MEB (0.15 s^{-1}), thereby highlighting the markedly enhanced intrinsic catalytic activity imparted by Mn incorporation.

The electrocatalyst's stability was evaluated using multi-step potential cycling, where the voltage was varied between 1.5 and 1.8 V before returning to 1.5 V after two cycles, as depicted in Fig. 3f. The Mn-MEB catalyst exhibits a rapid attainment of a stable state across the voltage increments and maintains a consistent performance throughout the duration of the test. Notably, there is minimal fluctuation observed in current density across multiple continuous voltages. Furthermore, the current density associated with the Mn-MEB catalyst material significantly exceeds that of the comparative samples, MEB and CoFeB, under equivalent voltage conditions. This demonstrates the superior stabilization capability of the OER process for the Mn-MEB catalyst. To assess long-term applicability, we evaluated the cycle stability of Mn-MEB. As depicted in Fig. 3g, Mn-MEB exhibited minimal fluctuation at a voltage of 1.51 V and retained 91 % of 10 mA cm^{-2} over 26 h. In comparison, as shown in **Fig. S15**, the MEB catalyst retained 61 %, while the CoFeB catalyst retained only 27 %. Interestingly, the electrolyte containing Mn-MEB remained clear and transparent after the same cycling time, whereas that with MEB showed significant powder formation due to electrode material shedding (**Fig. S16**). Therefore, Mn-MEB exhibited superior structural stability and stronger substrate binding, thereby enhancing its durability during the OER and outperforming the commercial RuO_2 catalyst (**Fig. S17**) [40].

2.3. Mechanistic insight

To verify the enhancement in intrinsic activity, we measured the OER activation energy through temperature-dependent OER

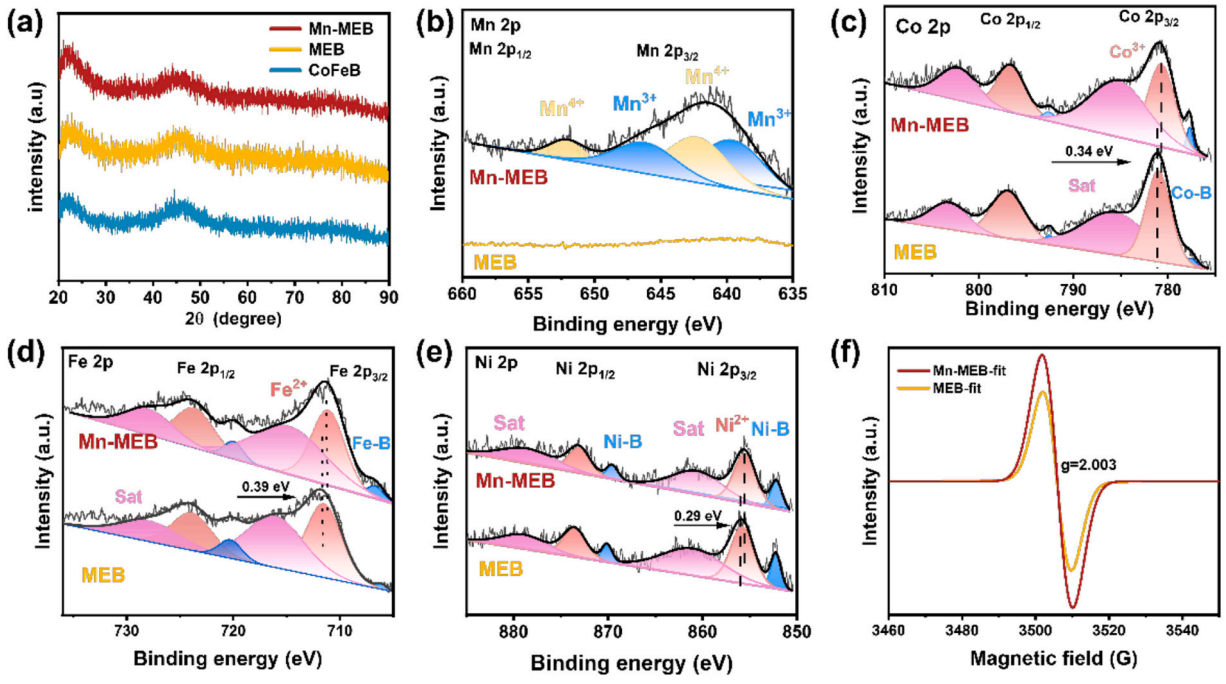

Fig. 2. (a) XRD patterns of CoFeB, MEB and Mn-MEB. XPS spectra of (b) Mn 2p, (c) Co 2p, (d) Fe 2p and (e) Ni 2p for MEB and Mn-MEB. (f) EPR spectra of Mn-MEB and MEB.

performance analysis. As illustrated in Fig. 4**a-b and S18**, both Mn-MEB and MEB exhibit increased OER currents and reduced onset potentials with rising temperatures. The Arrhenius plots at 1.64 V for Mn-MEB and MEB allowed for the calculation of electrochemical activation energies, which were in line with earlier studies (insets of Fig. 4**a-b**). The activation energy for Mn-MEB is 18.5 kJ mol^{-1}, notably lower than the 20.3 kJ mol^{-1} observed for MEB. The results indicate that incorporating Mn into the MEB structure significantly enhances OER performance, as demonstrated by the reduced overpotential required to overcome the kinetic barrier compared to the baseline MEB catalyst (Fig. 4**c**). Additionally, the Faradaic efficiency (FE) for both hydrogen and oxygen evolution reactions was assessed in an alkaline environment using an H-type electrolytic cell, demonstrating excellent selectivity toward the HER and OER processes. A Nafion membrane was employed in the electrolyzer to effectively separate the evolved O_2 and H_2 gases. As shown in **Fig. S19**, oxygen was collected in an orange cylinder and hydrogen in a yellow cylinder. The increase in gas volume within the cylinders was measured and recorded every 200 s once the electrolyzer reached a stable operating level. The actual volumes of hydrogen and oxygen collected were then compared with their theoretical values. The Faradaic efficiency of Mn-MEB was determined to be approximately 96 %, indicating robust hydrogen and oxygen production capabilities and confirming its efficiency as an electrocatalyst for water electrolysis in alkaline environments. Furthermore, the fitting curves reveal that the hydrogen-to-oxygen evolution rate ratio is nearly 2:1, underscoring the catalyst's potential for practical storage of intermittent energy (Fig. 4**d-e**).

For further insight into the enhanced OER performance of MEB and Mn-MEB catalyst, the 3d orbital behavior on their surfaces is illustrated in **Fig. S20 and Table S3**. The density of states (DOS) analysis is shown in Fig. 4**g-h**. The *d*-band center, defined as the weighted average energy of the transition metal *d* orbitals derived from the partial density of states (PDOS), reflects the electron occupancy near the Fermi level (E_f) [41]. Compared to MEB, the Mn-MEB structure exhibits a *d*-band center shifted by −2.3 eV closer to the Fermi level, indicating reduced adsorption energy for active intermediates and increased electron density. To elucidate charge transfer dynamics between metal and boron sites, we analyzed the p-d orbital overlap using PDOS data (**Fig. S21–22**). As shown in Fig. 4**f**, the 3d band of Mn-MEB spans a broader energy range than that of MEB, although its 3d-band center lies deeper below the Fermi level. This leads to stronger orbital overlap between metal 3d and boron 2p states in Mn-MEB. Additionally, spin polarization of the 3d orbitals was examined to evaluate the electronic behavior of spin states. The Mn-MEB system exhibits significantly stronger spin polarization than MEB, primarily due to the Ni 3d band, rather than contributions from the Fe 3d or Co 3d orbitals. (Fig. 4**i and S23**). The introduction of Mn regulates the electronic state of Ni active sites in MEB, consistent with the increase in the number of unpaired electrons observed by EPR. Consequently, incorporating manganese to modify the electronic structure of the Ni sites effectively enhances the OER activity.

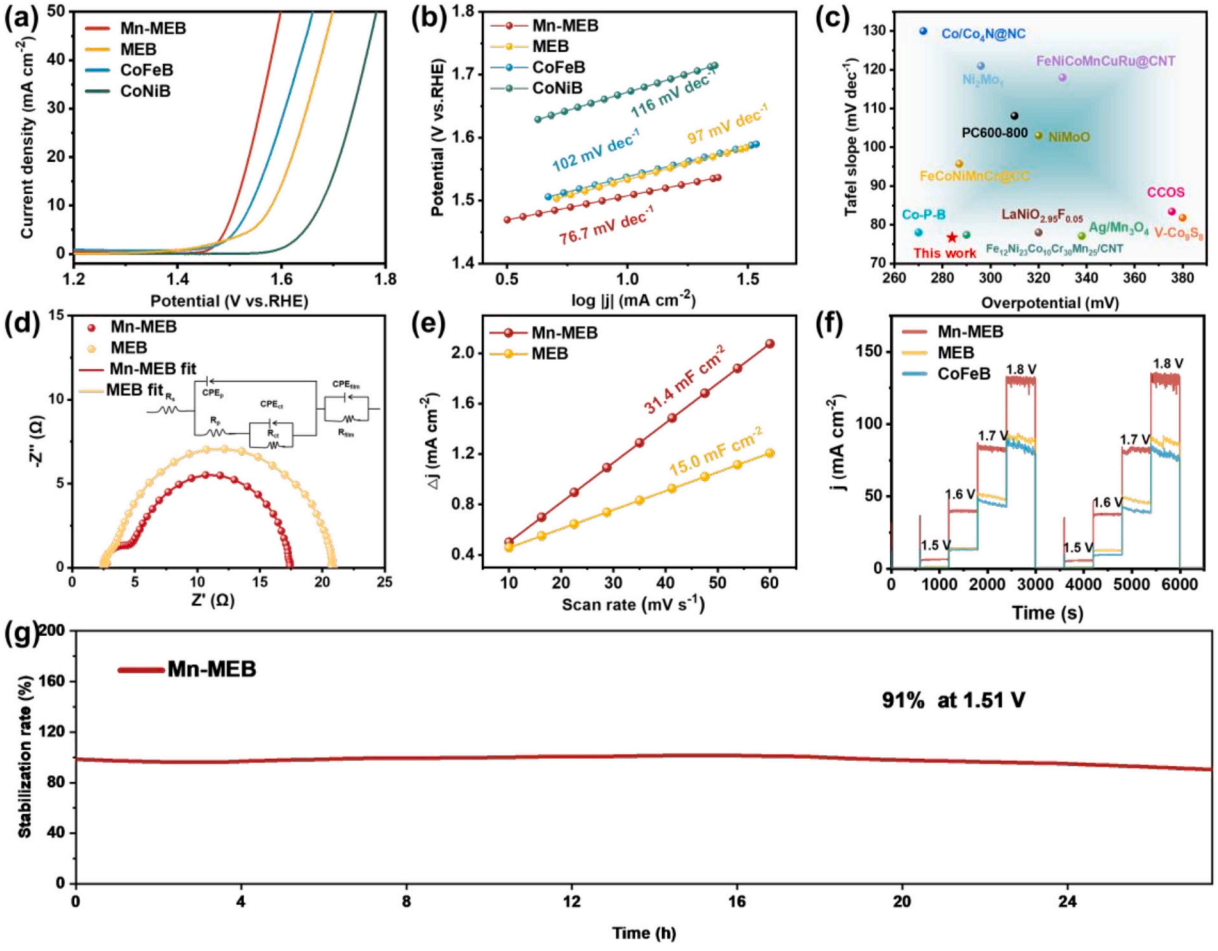

Fig. 3. (a) OER polarization curves, (b) Tafel plots. (c) OER performance comparison between Mn-MEB and other electrocatalysts at j = 10 mA cm^{-2} and Tafel slope. (d) Electrochemical impedance spectroscopy of Mn-MEB and MEB. (e) Electrochemical double-layer capacitor (C_{dl}) of Mn-MEB and MEB. (f) Multi-potential steps parameters plot of Mn-MEB, MEB and CoFeB. (g) Chronoamperometry stability of Mn-MEB.

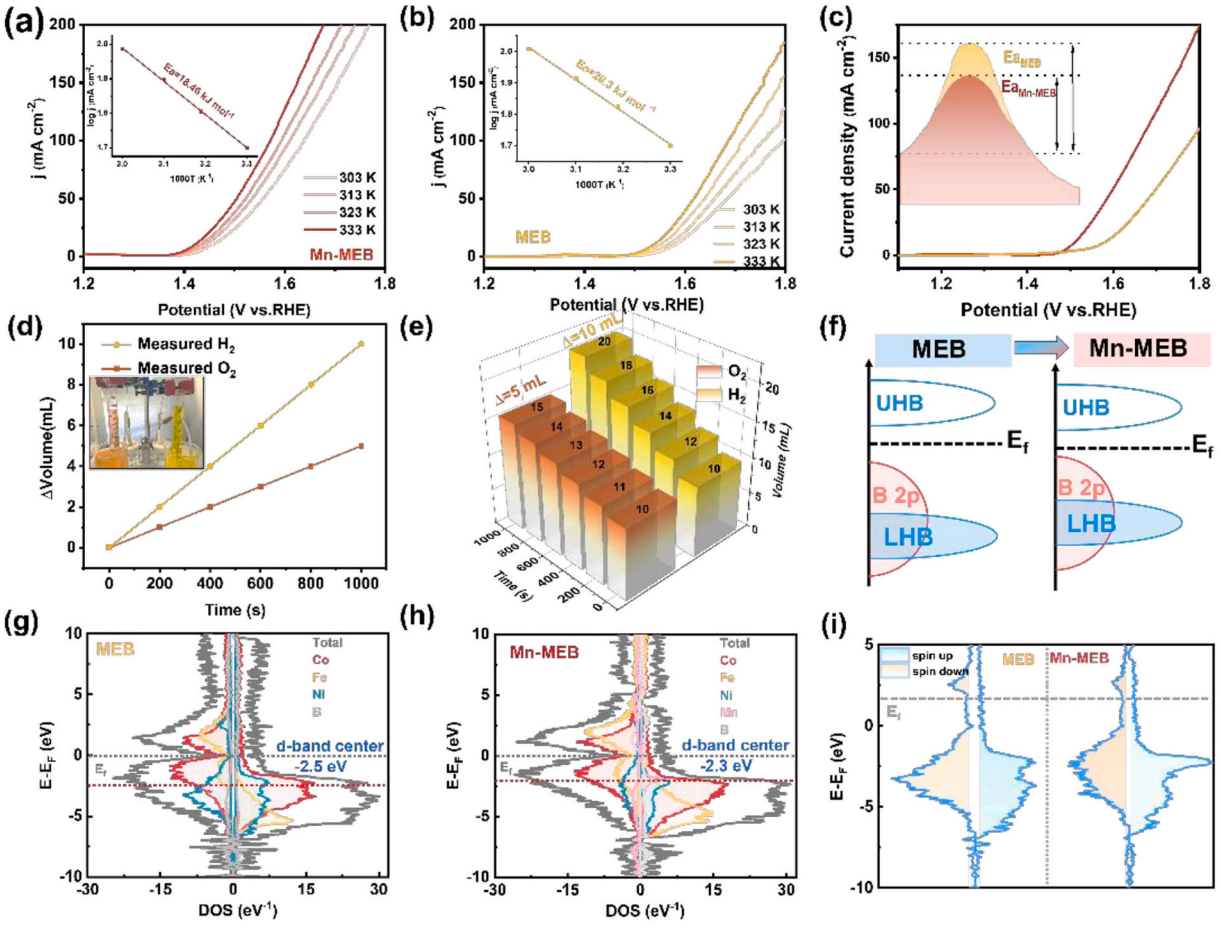

Fig. 4. (a-b) LSV measurements for Mn-MEB and MEB electrode measured from 303 to 333 K with an increment of 10 K (inset of image: Arrhenius-like plot of the current density). (c) Illustration of different activation energies for Mn-MEB and MEB. (d-e) Plot illustrating the volume of H_2 and O_2 gases. (f) Schematic energy bands of MEB and Mn-MEB. (g-h) Density of states of Mn-MEB and MEB. (i) Spin-polarization in Mn-MEB and MEB by the influence of Ni-3d band.

2.4. In-situ reconstruction and phase segregation during OER process

During the OER, metal species on the catalyst surface undergo in situ structural reconstruction. EIS is a valuable experimental technique for investigating the kinetics of electrocatalytic reactions and characterizing the electrode/electrolyte interface properties [42,43]. To monitor the behavior of adsorbed *OH intermediates at metal sites in Mn-MEB during the OER, operando EIS measurements were conducted, providing detailed insights into reaction kinetics in an alkaline electrolyte. The operando Bode plots indicate that the charge transfer responses can be categorized into two distinct frequency domains (Fig. 5a-b). At higher frequencies (10^2 to 10^4 Hz), the signal corresponds to electron transport within the internal structure of the catalyst, while the lower frequency range (10^{-2} to 10^2 Hz) reflects interfacial charge transfer between the catalyst and the electrolyte [44]. These findings, along with the associated Bode phase and Nyquist plots, were analyzed using a fitted equivalent circuit model (Fig. 5c) [45,46]. In this equivalent circuit model, R_s denotes the resistance of the electrolyte. The first parallel branch includes a constant phase element (CPE_p) and a resistance (R_p), which are associated with electron transport from the catalyst's interior to the active interface. Importantly, R_p also captures the effects of surface reconstruction occurring during the OER process. The second parallel network comprises another constant phase element (CPE_{ct}) and a charge transfer resistance (R_{ct}), representing interfacial electron transfer between the catalyst and the surrounding electrolyte [47]. The relatively smaller R_p value of Mn-MEB indicates more facile oxidation and structural reconstruction. In the low potential range (1.10–1.35 V), the R_p values of both MEB and Mn-MEB decline sharply, suggesting that rapid structural changes occur without the onset of OER activity. For Mn-MEB, a pronounced decrease in R_p above 1.35 V signifies the initiation of OER, whereas for MEB, this transition is observed only above 1.45 V. These findings underscore the superior OER kinetics and intrinsic catalytic activity of Mn-MEB (**Fig. S24**). The incorporation of Mn enhances the utilization of *OH intermediates, thereby improving charge transfer and deprotonation efficiency and ultimately accelerating the catalytic kinetics of water oxidation.

To elucidate the underlying cause of phase segregation occurring during the OER, the active phase of Mn-MEB under water oxidation conditions was investigated (**Fig. S25**). XPS and SAED analyses were employed to examine the compositional changes in Mn-MEB before and after cyclic voltammetry treatment. The SAED images revealed a distinct crystalline structure for Mn-MEB (**Fig. S26**). Specifically, the SAED patterns displayed diffraction rings corresponding to the (015) planes along with broad rings that confirm the coexistence of nanocrystalline NiCo layered double hydroxide (NiCo-LDH) [48]. Fig. 5d-f display the XPS spectra of Mn-MEB before and after CV. After CV, the XPS spectra of Co 2p, Fe 2p and Ni 2p exhibited noticeable shifts toward higher binding energies (Fig. 5d-f), along with an increased Co^{2+}/Co–B ratio, indicating the formation of Co hydroxide species on the Mn-MEB surface [49–56]. These results are consistent with previous studies showing that, under alkaline water electrolysis conditions, NiCo-based materials undergo surface reconstruction to form hydroxide phases such as $Ni(OH)_2$ and NiCo-LDH (**Fig. S27**), which are widely regarded as the true active species during the OER [57–60]. Compared to the untreated catalyst, the Mn 2p XPS peak shifts toward lower binding energies after CV (**Fig. S28**). Overall, the XPS results indicate that the cyclic voltammetry

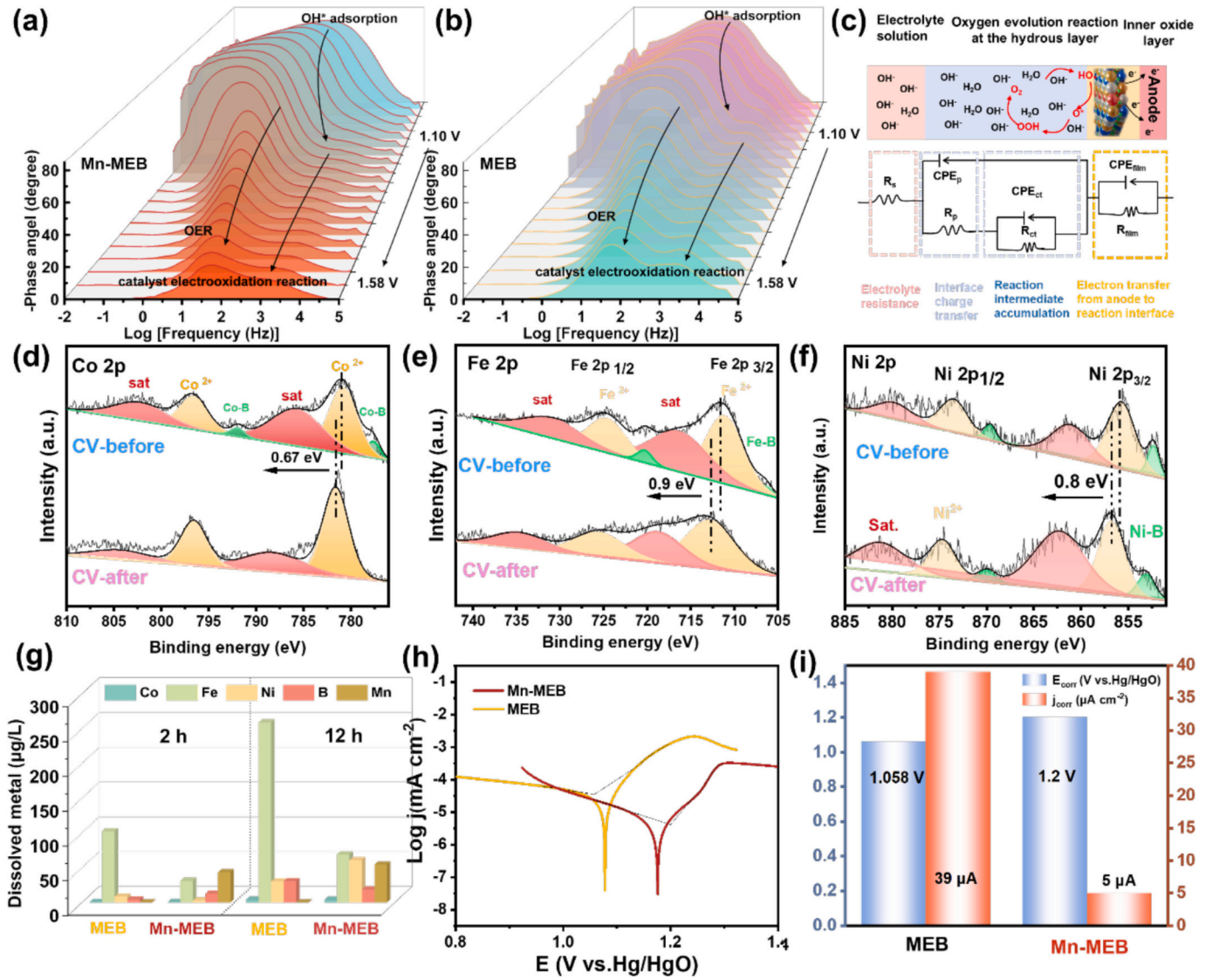

Fig. 5. Operando Bode phase angle plots for (a) Mn-MEB and (b) MEB catalysts. (c) Equivalent circuit model alongside a schematic illustrating the relationships among reaction intermediates. High-resolution XPS spectra of the (d) Co 2p, (e) Fe 2p and (f) Ni 2p regions for the Mn-MEB electrode before and after CV testing. (g) Time-dependent concentration of Co, Fe, Ni, B and Mn dissolved in the electrolyte during the CA test. (h) Potentiodynamic polarization curves. (i) Corrosion potentials (E_{corr}) and corrosion current densities (I_{corr}) of Mn-MEB and MEB.

treatment facilitates the formation of a NiCo-LDH interfacial layer on the MEB surface. This layer is instrumental in inhibiting phase segregation and structural transformation, thereby enhancing the catalyst's stability [61,62].

Elemental dissolution throughout the prolonged OER testing was tracked by analyzing the electrolyte composition via ICP-MS, as shown in Fig. 5g. In the first 2 h of operation, the dissolution of all elements in the Mn-MEB catalyst was measured at 91.74 μg/L, significantly lower than the dissolution observed in the MEB catalyst. After 12 h of OER operation, the disparity in dissolution across all elements became more pronounced: Mn-MEB showed only a 60.93 μg/L (only 66 % rise), while MEB exhibited a 207.65 μg/L (178 % rise). These findings suggest that manganese incorporation effectively inhibits all elements dissolution, thereby explaining the notably superior stability of Mn-MEB compared to MEB [63]. Minimizing metal leaching aligns the catalyst design with green chemistry principles, thereby enhancing both resource efficiency and environmental sustainability. The corrosion resistance of materials is typically assessed using two key electrochemical parameters: corrosion current density and corrosion potential (Fig. 5h-i) [64]. The Mn-MEB electrode exhibited a higher corrosion potential (1.200 V vs. Hg/HgO) and a significantly lower corrosion current (5 μA cm^{-2}) compared to the MEB electrode, which showed a corrosion current of 96 μA cm^{-2} at 1.058 V vs. Hg/HgO [65]. A higher corrosion potential signifies that the electrode undergoes corrosion at a higher potential, while a lower corrosion current reflects a reduced rate of corrosion [66]. These results demonstrate the enhanced corrosion resistance of the Mn-MEB electrode compared to the undoped MEB [33]. The incorporation of Mn is shown to effectively suppress Fe leaching and phase separation, which collectively contribute to enhanced structural integrity and long-term catalytic durability [67]. These improvements can be attributed to the "slow diffusion effect" [68] and the "cocktail effect" observed in high-entropy boride materials (**Fig. S29**) [69].

2.5. AEMWE performance

A water-splitting device based on an anion exchange membrane (AEMWE) was constructed, employing E130-type Raney nickel mesh as the cathodic material and Mn-MEB as the anodic material (Fig. 6a). As illustrated in Fig. 6b, polarization measurements were conducted at 60°C. The E130(+)||Mn-MEB(−) cell demonstrated superior

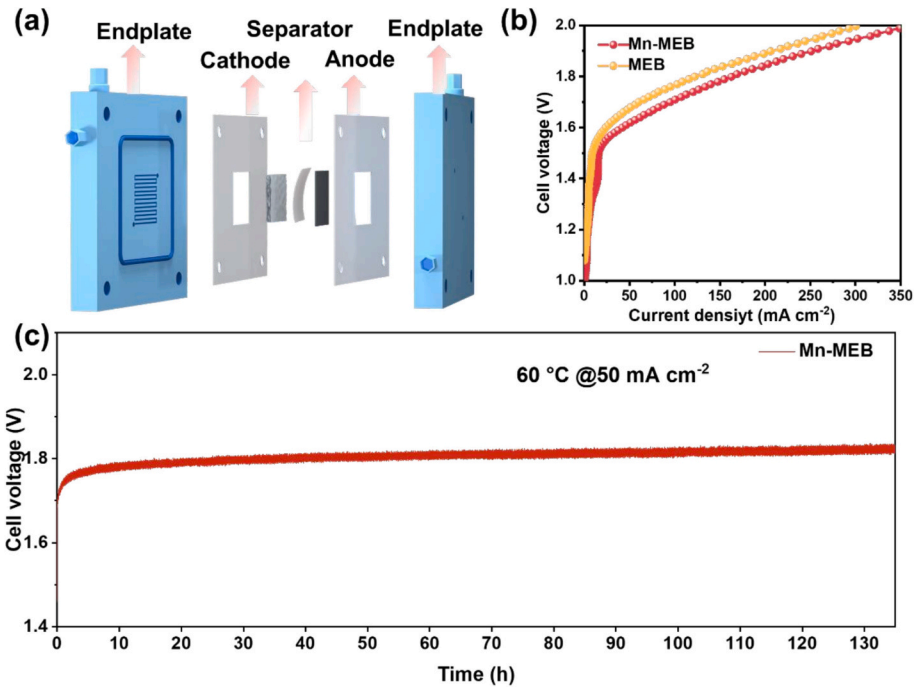

Fig. 6. (a) Schematic diagram of the anion exchange membrane water electrolyzer (AEMWE). (b) I-V curves of AEMWE for the prepared Mn-MEB and MEB as anodes in 1 M KOH electrolyte at 60 °C. (c) Chronopotentiometry curve of the Mn-MEB catalyst at a constant current density of 50 mA cm^{-2} in the AEMWE at 60 °C.

performance, requiring just 1.35 V to reach a current density of 10 mA cm^{-2}, in contrast to the 1.51 V needed by the E130(+)||MEB(−) assembly. Furthermore, long-term stability testing at 50 mA cm^{-2} demonstrated that the Mn-MEB exhibited excellent durability, with no significant voltage degradation over 135 h (Fig. 6c). The estimated operating cost of the Mn-MEB-based AEMWE was $0.88 and $0.93 per kg H_2 at 50 and 100 mA cm^{-2}, respectively, meeting the target set by the U.S. DOE (<$2 per kg H_2) [70]. Overall, the outstanding stability and low operational cost of Mn-MEB highlight its strong potential for industrial application.

3. Conclusion

We have successfully developed a magnetic field-assisted Mn incorporation strategy to construct medium-entropy metal boride (Mn-MEB) nanochains with simultaneously enhanced OER activity and stability. The Mn-MEB catalyst delivers a low overpotential of 280 mV at 10 mA cm^{-2} and remarkable long-term durability without performance degradation. Mechanistic investigations reveal that Mn incorporation synergistically modulates the electronic structure of Ni active sites, optimizing intermediate adsorption energies and facilitating efficient catalytic processes. In parallel, the increased configurational entropy suppresses phase segregation and promotes the formation of a robust hydroxide layer, contributing to superior structural integrity under electrochemical conditions. When employed in an AEMWE, the Mn-MEB anode achieves a low cell voltage of 1.35 V at 10 mA cm^{-2} and maintains stable operation over 130 h. Our work proposes a rational design strategy that leverages the configurational entropy effect and regulates active sites to enhance the OER performance of catalysts.

CRediT authorship contribution statement

Yafeng Li: Data curation. **Lin Wu:** Formal analysis. **Shuai Chen:** Formal analysis. **Meijia Liu:** Data curation. **Yuhang Lei:** Writing – original draft, Data curation. **Shuxin Li:** Writing – original draft. **Lin Tao:** Writing – original draft. **Lixiang Li:** Writing – original draft. **Chengguo Sun:** Writing – original draft. **Han Zhang:** Writing – review & editing, Writing – original draft, Funding acquisition. **Baigang An:** Writing – original draft, Funding acquisition.

Declaration of competing interest

The authors declare that they have no known competing financial interests or personal relationships that could have appeared to influence the work reported in this paper.

Acknowledgements

The authors gratefully acknowledge financial supported by the National Natural Science Foundation of China (22109061, 11972178, 51972156 and 52304330), the Nature Science Foundation of Liaoning Province (2022-BS-283), and Technology Liaoning Project Grants (601010326). Key Project supported by the Research Foundation of Education Bureau of Liaoning Province (No. JYTZD2023093), Distinguished Professor Project of Education Department of Liaoning and the Open Project Found of Key Laboratory of Energy Materials and Electrochemistry Liaoning Province are acknowledged. Liaoning University of Science and Technology Graduate Innovation and Entrepreneurship Project (No. LKDYC202303) are acknowledged.

Appendix A. Supplementary data

Supplementary data to this article can be found online at https://doi.org/10.1016/j.jcis.2025.138682.

Data availability

The data supporting this article have been included as part of the Supplementary Information. All data included in this study are available upon request by contact with the corresponding author.

References

[1] Z.W. Seh, J. Kibsgaard, C.F. Dickens, I. Chorkendorff, J.K. Nørskov, T.F. Jaramillo, Combining theory and experiment in electrocatalysis: insights into materials design, Science 355 (6321) (2017) eaad4998.

[2] M.P. Browne, Z. Sofer, M. Pumera, Layered and two dimensional metal oxides for electrochemical energy conversion, Energy Environ. Sci. 12 (1) (2019) 41–58.

[3] C. Wang, L. Jin, H. Shang, H. Xu, Y. Shiraishi, Y. Du, Advances in engineering RuO_2 electrocatalysts towards oxygen evolution reaction, Chin. Chem. Lett. 32 (7) (2021) 2108–2116.

[4] J. Qian, T. Wang, Z. Zhang, Y. Liu, J. Li, D.J.N.E. Gao, Engineered spin state in Ce doped $LaCoO_3$ with enhanced electrocatalytic activity for rechargeable Zn-air batteries, Nano Energy 74 (2020) 104948.

[5] K. Wu, K. Sun, S. Liu, W.-C. Cheong, Z. Chen, C. Zhang, Y. Pan, Y. Cheng, Z. Zhuang, X. Wei, Atomically dispersed Ni-Ru-P interface sites for high-efficiency pH-universal electrocatalysis of hydrogen evolution, Nano Energy 80 (2021) 105467.

[6] M. Wang, L. Zhang, J. Pan, M. Huang, H. Zhu, A highly efficient Fe-doped Ni_3S_2 electrocatalyst for overall water splitting, Nano Res 14 (2021) 4740–4747.

[7] L. Zeng, Z. Liu, K. Sun, Y. Chen, J. Zhao, Y. Chen, Y. Pan, Y. Lu, Y. Liu, C. Liu, Multiple modulations of pyrite nickel sulfides via metal heteroatom doping engineering for boosting alkaline and neutral hydrogen evolution, J Mater Chem A 7 (44) (2019) 25628–25640.

[8] B. Zhang, C. Xiao, S. Xie, J. Liang, X. Chen, Y. Tang, Iron–nickel nitride nanostructures in situ grown on surface-redox-etching nickel foam: efficient and ultrasustainable electrocatalysts for overall water splitting, Chem. Mater. 28 (19) (2016) 6934–6941.

[9] Z. Chen, Y. Song, J. Cai, X. Zheng, D. Han, Y. Wu, Y. Zang, S. Niu, Y. Liu, J. Zhu, Tailoring the d-band centers enables Co4N nanosheets to be highly active for hydrogen evolution catalysis, Angew. Chem. Int. Ed. 57 (18) (2018) 5076–5080.

[10] H. Fan, H. Yu, Y. Zhang, Y. Zheng, Y. Luo, Z. Dai, B. Li, Y. Zong, Q. Yan, Fe-doped Ni_3C nanodots in N-doped carbon nanosheets for efficient hydrogen-evolution and oxygen-evolution electrocatalysis, Angew. Chem. Int. Ed. 56 (41) (2017) 12566–12570.

[11] T.Y. Ma, J.L. Cao, M. Jaroniec, S.Z. Qiao, Interacting carbon nitride and titanium carbide nanosheets for high-performance oxygen evolution, Angew. Chem. Int. Ed. 55 (3) (2016) 1138–1142.

[12] P. Aghamohammadi, B. Hüner, O.C. Altıncı, E.T. Akgul, B. Teymur, U.B. Simsek, M. Demir, Recent advances in the electrocatalytic applications (HER, OER, ORR, water splitting) of transition metal borides (MBenes) materials, Int. J. Hydrogen Energy 87 (2024) 179–198.

[13] Y. Yao, Z. Zhang, L. Jiao, Development strategies in transition metal borides for electrochemical water splitting, Energy&Environmental Materials 5 (2) (2022) 470–485.

[14] N. Wang, A. Xu, P. Ou, S.-F. Hung, A. Ozden, Y.-R. Lu, J. Abed, Z. Wang, Y. Yan, M.-J. Sun, Y. Xia, M. Han, J. Han, K. Yao, F.-Y. Wu, P.-H. Chen, A. Vomiero, A. Seifitokaldani, X. Sun, D. Sinton, Y. Liu, E.H. Sargent, H. Liang, Boride-derived oxygen-evolution catalysts, Nat. Commun. 12 (1) (2021) 6089.

[15] D. Feng, Y. Dong, P. Nie, L. Zhang, Z.-A. Qiao, CoNiCuMgZn high entropy alloy nanoparticles embedded onto graphene sheets via anchoring and alloying strategy as efficient electrocatalysts for hydrogen evolution reaction, Chem. Eng. J. 430 (2022) 132883.

[16] L. Peng, N. Yang, Y. Yang, Q. Wang, X. Xie, D. Sun-Waterhouse, L. Shang, T. Zhang, G.I.N. Waterhouse, Atomic cation-vacancy engineering of NiFe-layered double hydroxides for improved activity and stability towards the oxygen evolution reaction, Angew. Chem. Int. Ed. 60 (46) (2021) 24612–24619.

[17] S. Dong, H. Zhou, X. Hu, J. Zhang, Y. Li, W. Shang, Z. Liu, L. Wan, H. Zhao, Application of transition metal high entropy boride in electrocatalytic hydrogen evolution reaction, Int. J. Hydrogen Energy 48 (48) (2023) 18233–18244.

[18] B. Post, F.W. Glaser, D. Moskowitz, Transition metal diborides, Acta Metall. 2 (1) (1954) 20–25.

[19] D.B. Tripathy, Novel two-dimensional MBenes: synthesis, properties, and energy storage and electrocatalytic applications of two-dimensional metal borides, ACS Applied Engineering Materials 2 (5) (2024) 1209–1224.

[20] Z. Chen, R. Zheng, M. Graś, W. Wei, G. Lota, H. Chen, B.-J. Ni, Tuning electronic property and surface reconstruction of amorphous iron borides via WP co-doping for highly efficient oxygen evolution, Appl. Catal. Environ. 288 (2021) 120037.

[21] J. Greeley, M. Mavrikakis, Alloy catalysts designed from first principles, Nat. Mater. 3 (11) (2004) 810–815.

[22] Y. Yao, Q. Dong, A. Brozena, J. Luo, J. Miao, M. Chi, C. Wang, I.G. Kevrekidis, Z. J. Ren, J. Greeley, High-entropy nanoparticles: synthesis-structure-property relationships and data-driven discovery, Science 376 (6589) (2022) eabn3103.

[23] S. Ahmad, M. Egilmez, W. Abuzaid, F. Mustafa, A.M. Kannan, A.S. Alnaser, Efficient medium entropy alloy thin films as bifunctional electrodes for electrocatalytic water splitting, Int. J. Hydrogen Energy 52 (2024) 1428–1439.

[24] Y. Shao, J. Ni, J. Yin, X. Liu, S. Guo, Y. Xu, B. Song, Y. Song, X. Li, L. Luo, Fe-rich medium-entropy Core-Shell electrocatalyst for hydrogen evolution reaction under large current density, Small 21 (4) (2025) 2407061.

[25] H. Lv, Z. Ye, F. Pei, X. Peng, J. Huang, D. Li, Z. Jin, Increased oxygen evolution activity in pH-universal electrocatalyst: urea-modified NiFeCoCN medium-entropy alloy, Chin. J. Chem. 41 (23) (2023) 3290–3298.

[26] B. Wang, X. Zhu, X. Pei, W. Liu, Y. Leng, X. Yu, C. Wang, L. Hu, Q. Su, C. Wu, Room-temperature laser planting of high-loading single-atom catalysts for high-efficiency electrocatalytic hydrogen evolution, J. Am. Chem. Soc. 145 (25) (2023) 13788–13795.

[27] Y. Li, B. Huang, Y. Sun, M. Luo, Y. Yang, Y. Qin, L. Wang, C. Li, F. Lv, W. Zhang, S. Guo, Multimetal borides nanochains as efficient electrocatalysts for overall water splitting, Small 15 (1) (2019) e1804212.

[28] F. Li, Y. Ma, H. Wu, Q. Zhai, J. Zhao, H. Ji, S. Tang, X. Meng, Sub-3-nm high-entropy metal Sulfide nanoparticles with synergistic effects as promising electrocatalysts for enhanced oxygen evolution reaction, J. Phys. Chem. C 126 (43) (2022) 18323–18332.

[29] J. Masa, P. Weide, D. Peeters, I. Sinev, W. Xia, Z. Sun, C. Somsen, M. Muhler, W. Schuhmann, Amorphous cobalt boride (Co_2B) as a highly efficient nonprecious catalyst for electrochemical water splitting: oxygen and hydrogen evolution, Adv. Energy Mater. 6 (6) (2016) 1502313.

[30] H. Han, Y.R. Hong, J. Woo, S. Mhin, K.M. Kim, J. Kwon, H. Choi, Y.C. Chung, T. Song, Electronically double-layered metal boride hollow nanoprism as an excellent and robust water oxidation electrocatalysts, Advanced Energy Materials 9 (13) (2019) 1803799.

[31] B. Jiang, K. Liang, Z. Yang, K. Guo, F. Shaik, J. Zheng, FeCoNiB@boron-doped vertically aligned graphene arrays: a self-supported electrocatalyst for overall water splitting in a wide pH range, Electrochim. Acta 386 (2021) 138459.

[32] F.-G. Wang, B. Liu, H.-Y. Wang, Z.-Y. Lin, Y.-W. Dong, N. Yu, R.-N. Luan, Y.-M. Chai, B. Dong, Motivating borate doped FeNi layered double hydroxides by molten salt method toward efficient oxygen evolution, J. Colloid Interface Sci. 610 (2022) 173–181.

[33] Y. Luo, P. Wang, G. Zhang, S. Wu, Z. Chen, H. Ranganathan, S. Sun, Z. Shi, Mn-doped nickel–iron phosphide heterointerface nanoflowers for efficient alkaline freshwater/seawater splitting at high current densities, Chem. Eng. J. 454 (2023) 140061.

[34] S. Gupta, M. Forster, A. Yadav, A.J. Cowan, N. Patel, M. Patel, Highly efficient and selective metal oxy-boride electrocatalysts for oxygen evolution from alkali and saline solutions, ACS Appl Energy Mater 3 (8) (2020) 7619–7628.

[35] S. Liu, Y. Shi, L. Xu, W. Zhan, M. Chen, X. Pan, Y. Yao, J. Cai, M. Zhang, X. Ma, Special $NaBH_4$ hydrolysis achieving multiple-surface-modifications promotes the high-throughput water oxidation of CoN nanowire arrays, Dalton Trans. 52 (28) (2023) 9714–9720.

[36] W. Fang, H. Wang, Z. Zhu, W. Qian, L. Qiu, W. Fan, J. Xiang, C. Yin, S. Chen, J. Wu, Doping Ni into CoB achieves surface reconstruction to promote efficient electrocatalytic hydrogen evolution reaction, Fuel 361 (2024) 130720.

[37] R. Sukanya, S.-M. Chen, Amorphous cobalt boride nanosheets anchored surface-functionalized carbon nanofiber: an bifunctional and efficient catalyst for electrochemical sensing and oxygen evolution reaction, J. Colloid Interface Sci. 580 (2020) 318–331.

[38] S. Wang, W. Huo, F. Fang, Z. Xie, J.K. Shang, J. Jiang, High entropy alloy/C nanoparticles derived from polymetallic MOF as promising electrocatalysts for alkaline oxygen evolution reaction, Chem. Eng. J. 429 (2022) 132410.

[39] L. Sharma, N.K. Katiyar, A. Parui, R. Das, R. Kumar, C.S. Tiwary, A.K. Singh, A. Halder, K. Biswas, Low-cost high entropy alloy (HEA) for high-efficiency oxygen evolution reaction (OER), Nano Res 15 (6) (2022) 4799–4806.

[40] I.N. Uzgoren, B. Huner, S. Yıldırım, et al., Development of IrO_2-WO_3 composite catalysts from waste WC-co wire drawing die for PEM water electrolyzers' oxygen evolution reactions, ACS Sustainable Chem. Eng. 10 (39) (2022) 13100–13111.

[41] M. Zhang, K. Luo, Y. Fan, X. Lu, J. Ye, N. Lu, J. Dong, Q. Niu, J. Zhang, P. Zhang, Metal vacancies and self-reconstruction of high entropy metal borates to boost the oxygen evolution reaction, Chem. Eng. J. 493 (2024) 152758.

[42] M.E. Lyons, M.P. Brandon, The significance of electrochemical impedance spectra recorded during active oxygen evolution for oxide covered Ni, co and Fe electrodes in alkaline solution, J. Electroanal. Chem. 631 (1–2) (2009) 62–70.

[43] R. Doyle, M. Lyons, Kinetics and mechanistic aspects of the oxygen evolution reaction at hydrous iron oxide films in base, J. Electrochem. Soc. 160 (2) (2013) H142.

[44] X. Zhang, C. Feng, B. Dong, C. Liu, Y. Chai, High-voltage-enabled stable cobalt species deposition on MnO_2 for water oxidation in acid, Adv. Mater. 35 (13) (2023) 2207066.

[45] A. Puntambekar, N. Chandrasekeran, Q. Wang, I. Roy, V. Premkumar, V. Chakrapani, Interaction of native defects with ions and its role in inducing phase transitions in p-type s-excess MoS_2, ACS Appl Energy Mater 1 (7) (2018) 3093–3102.

[46] J. Li, H.-X. Liu, W. Gou, M. Zhang, Z. Xia, S. Zhang, C.-R. Chang, Y. Ma, Y. Qu, Ethylene-glycol ligand environment facilitates highly efficient hydrogen evolution of Pt/CoP through proton concentration and hydrogen spillover, Energ. Environ. Sci. 12 (7) (2019) 2298–2304.

[47] J. Zhang, J. Liu, L. Zhang, J. Ke, C. Zhong, Y. Tu, L. Wang, H. Song, L. Du, Z. Zhang, Fe^{3+}-preactivated Ni/co-based antiperovskite nitrides for boosting oxygen evolution: surface tuning and catalytic mechanism, ACS Catal. 13 (7) (2023) 5043–5052.

[48] Y. Zhang, X. Song, S. Xue, Y. Liang, H. Jiang, Fabrication of hierarchically structured S-doped NiFe hydroxide/oxide electrodes for solar-assisted oxygen evolution reaction in seawater splitting, Appl. Catal. A Gen. 649 (2023) 118965.

[49] Q. Mao, K. Deng, H. Yu, Y. Xu, Z. Wang, X. Li, L. Wang, H. Wang, In situ reconstruction of partially hydroxylated porous rh metallene for ethylene glycol-assisted seawater splitting, Adv. Funct. Mater. 32 (31) (2022) 2201081.

[50] D. Sui, R. Luo, S. Xie, H. Zhang, T. Ma, H. Sun, T.-T. Jia, J. Sun, X. Li, Atomic ruthenium doping in collaboration with oxygen vacancy engineering boosts the hydrogen evolution reaction by optimizing H absorption, Chem. Eng. J. 480 (2024) 148007.

[51] Q. Liu, X. Fu, H. Li, J. Xing, W. Xiao, Y. Zong, G. Fu, J. Wang, Q. Cao, T. Ma, Microwave quasi-solid-constructed Ni_2P-$Ni_{12}P$ 5-supported Os with unique

metal–support interaction for anion-exchange membrane seawater electrolysis, Chem. Sci. 16 (2025) 13306–13315.
[52] Y. Wang, J. Li, P. Yang, H. Li, G. Xu, Y. Du, C. Li, W. Jin, T. Ma, Z. Wu, Interfacial Ru nanoclusters in tandem with single atoms on oxygen-vacancy regulated CeO_2 for anion exchange membrane seawater-splitting, J. Energy Chem. 102 (2025) 618–627.
[53] Y. Ou, L. Liu, X. Peng, L. Zhang, Z. Ou, W. Zhang, Y. Zhang, Structure transformation induced bi-component co-Mo/A-co$(OH)_2$ as highly efficient hydrogen evolution catalyst in alkaline media, Nano Materials Science 6 (5) (2024) 565–575.
[54] R. Deng, M. Guo, C. Wang, Q. Zhang, Recent advances in cobalt phosphide-based materials for electrocatalytic water splitting: from catalytic mechanism and synthesis method to optimization design, Nano Materials Science 6 (2) (2024) 139–173.
[55] Y.N. Zhou, W.L. Yu, H.J. Liu, R.Y. Fan, G.Q. Han, B. Dong, Y.M. Chai, Self-integration exactly constructing oxygen-modified MoNi alloys for efficient hydrogen evolution, EcoEnergy 1 (2) (2023) 425–436.
[56] M.S.A. Sher Shah, G.Y. Jang, K. Zhang, J.H.J.E. Park, Transition metal carbide-based nanostructures for electrochemical hydrogen and oxygen evolution reactions, EcoEnergy 1 (2) (2023) 344–374.
[57] Y. Xin, Q. Hua, C. Li, H. Zhu, L. Gao, X. Ren, P. Yang, A. Liu, Enhancing electrochemical performance and corrosion resistance of nickel-based catalysts in seawater electrolysis: focusing on OER and HER, J Mater Chem A 12 (35) (2024) 23147–23178.
[58] Q. Zhang, W. Xiao, H.C. Fu, X.L. Li, J.L. Lei, H.Q. Luo, N.B. Li, Unraveling the mechanism of self-repair of NiFe-based electrocatalysts by dynamic exchange of iron during the oxygen evolution reaction, ACS Catal. 13 (22) (2023) 14975–14986.
[59] J. Han, S. Jiao, J. Sun, H. Qi, C. Hou, J. Guan, In-depth investigation on the influence of iron impurity on the oxygen evolution performance of iron-based catalysts, Int. J. Hydrogen Energy 49 (2024) 1022–1029.
[60] Y.-C. Zhang, C. Han, J. Gao, L. Pan, J. Wu, X.-D. Zhu, J.-J. Zou, NiCo-based electrocatalysts for the alkaline oxygen evolution reaction: a review, ACS Catalysis 11 (20) (2021) 12485–12509.
[61] Z. Wang, J. Zhang, Q. Wei, F. Guo, R. Chen, H. Jiang, W. Wu, Y. Zhu, S. Chen, Y. Wang, Tailored electronic interaction between metal-support trigger reverse hydrogen spillover for efficient hydrogen evolution, J. Colloid Interface Sci. (2025).
[62] R. Chen, Y. Yang, W. Wu, S. Chen, Z. Wang, Y. Zhu, N. Cheng, Reconstructed β-NiOOH enabling highly efficient and ultrastable oxygen evolution at large current density, Chem. Eng. J. 480 (2024) 148100.
[63] X. Wang, Y. Zuo, S. Horta, R. He, L. Yang, A. Ostovari Moghaddam, M. Ibáñez, X. Qi, A. Cabot, CoFeNiMnZnB as a high-entropy metal boride to boost the oxygen evolution reaction, ACS Appl. Mater. Interfaces 14 (42) (2022) 48212–48219.
[64] J. Jiang, Y. Tian, J. Zhang, C. Zhang, L. Ai, Metallic cu-incorporated NiFe layered double hydroxide nanosheets enabling energy-saving hydrogen generation from chlorine-free seawater electrolysis coupled with sulfion upcycling, Fuel 367 (2024) 131506.
[65] L. Ye, Y. Ding, X. Niu, X. Xu, K. Fan, Y. Wen, L. Zong, X. Li, X. Du, T. Zhan, Unraveling the crucial contribution of additive chromate to efficient and stable alkaline seawater oxidation on Ni-based layered double hydroxides, J. Colloid Interface Sci. 665 (2024) 240–251.
[66] L. Yang, Y. Zhao, L. Zhu, D. Xia, Rational construction of grille structured P-CoZnO-Cu_2SeS/NF composite electrocatalyst for boosting seawater electrolysis and corrosion resistance, Appl. Surf. Sci. 631 (2023) 157541.
[67] D. Liu, X. Yan, P. Guo, Y. Yang, Y. He, J. Liu, J. Chen, H. Pan, R. Wu, Inert Mg incorporation to break the activity/stability relationship in high-entropy layered hydroxides for the electrocatalytic oxygen evolution reaction, ACS Catal. 13 (11) (2023) 7698–7706.
[68] Q. Wang, J. Xie, Y. Qin, Y. Kong, S. Zhou, Q. Li, Q. Sun, B. Chen, P. Xie, Z. Wei, S. Zhao, Recent progress in high-entropy alloy electrocatalysts for hydrogen evolution reaction, Adv. Mater. Interfaces 11 (14) (2024) 2301020.
[69] L. Wang, L. Zhang, X. Lu, F. Wu, X. Sun, H. Zhao, Q. Li, Surprising cocktail effect in high entropy alloys on catalyzing magnesium hydride for solid-state hydrogen storage, Chem. Eng. J. 465 (2023) 142766.
[70] Z. Shi, J. Li, Y. Wang, S. Liu, J. Zhu, J. Yang, X. Wang, J. Ni, Z. Jiang, L. Zhang, Customized reaction route for ruthenium oxide towards stabilized water oxidation in high-performance PEM electrolyzers, Nat. Commun. 14 (1) (2023) 843.